CONTROLLED STRAIN OF CARDIAC MICROTISSUE VIA MAGNETIC ACTUATION

Josh Javor, Subramanian Sundaram, Christopher Chen, and David J. Bishop Boston University, Boston, Massachusetts 02215

ABSTRACT

This work presents a microscale tissue testbed with closed loop mechanical control. The platform leverages a non-contact technique capable of simultaneous actuation and detection, both derived from magnetic fields. We demonstrate cyclic tension and compression of engineered microtissue as well as long-term monitoring of spontaneous beating inside an incubator. The device is capable of positional feedback with high spatial and temporal resolution, while maintaining optical access from a standard microscope. Such a platform will enable experimental design of arbitrary mechanical environments for tissue conditioning, maturation, and monitoring.

KEYWORDS

Maturation, cardiac tissue engineering, mechanical pacing, monitoring, BioMEMS, microtissue, organ-on-a-chip, hiPSC, feedback control

INTRODUCTION

Mechanical forces play a significant role in the function and maturation of all biological tissues [1]. For the field of tissue engineering, maturation is critical for physiologically relevant toxicity testing, disease modeling, and – eventually – tissue replacement. Recently, the role of mechanics has been directly linked to the maturation of human induced pluripotent stem cell-derived (hiPSC) cardiac tissue [2,3]. The development of biocompatible, microscale platforms has been instrumental in the study and design of this mechanical environment [4-7]. Magnetic actuation and detection have specific advantages for the development of non-contact, remote control in organ-on-achip platforms. Previous work has achieved unidirectional strain in hiPSC-derived microtissues [6] as well as noncontact strain sensing in larger hiPSC-derived tissues [7]. Others have magnetically functionalized a 2D environment to tune substrate stiffness over long durations [8]. This work expands significantly on these ideas to develop a biocompatible platform with non-contact control, bidirectional strain, simultaneous actuation and sensing, and the potential for closed loop feedback (Fig. 1). Such a platform opens the design space substantially for biological experiments to understand the role of the mechanical environment.

FABRICATION

Elastomeric Microstructure

In essence, the device in Fig. 2a (red box) consists of magnetically functionalized microtissue strain gauge (μ TUG) inspired by Boudou, et. al [9]. A mold is designed in-house (SolidWorks) and 3D printed with dial-in tolerance (Protolabs). The mold is silanized overnight (Trichlorosilane, Sigma Aldrich) in vacuum to increase mold hydrophobicity and prevent elastomer sticking during removal. The platform material is polydimethylsiloxane (PDMS, Sylgard 184, Ellsworth), mixed in a 1:20 ratio of crosslinker to base. PDMS is mixed and poured into the

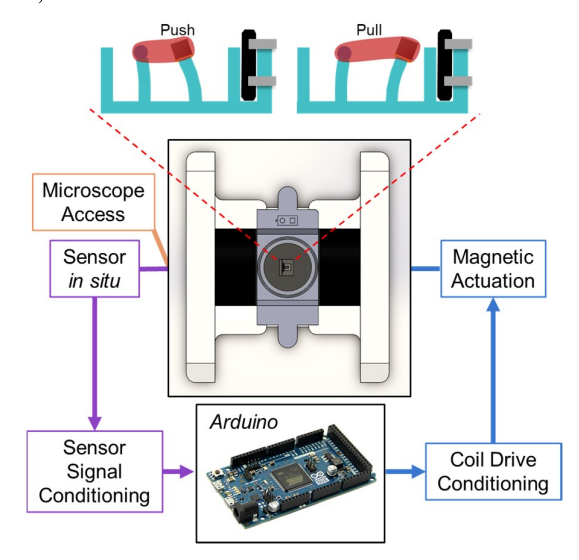


Figure 1: Platform offers experimental design with non-contact, cyclic magnetic actuation of microtissues, and simultaneous detection via closed-loop control.

mold before being degassed for 2 hours. The mold cures overnight at 60 °C and is carefully removed to keep micropillars intact. The cured structure in Fig. 2b consists of a small, rectangular well (5.5 μ L). Extruded from the base of the small well are two 800 μ m tall pillars (h), separated 1.2 mm center-to-center (d), with 390 μ m (w) by 430 μ m (t) rectangular cross sections. The primary direction of deflection occurs along the thinner side-length (w). On the top of one pillar is a PDMS sphere of diameter 490 μ m, which facilitates hydrogel attachment.

Magnetic Functionalization and Tissue Culture

The flat-top pillar is functionalized with micromagnet using a custom vacuum pick-and-place system, as illustrated in Fig. 2c-d. This system was previously developed for higher resolution fabrication on post-release silicon micro devices [10]. The micromagnet is a neodymium-iron-boron cube with 500 µm side length, N52 magnetization strength, and a typical outer coating of nickel (SM Magnetics). The micromagnets are passivated with 40 nm alumina using atomic layer deposition (GEMStar), where thicknesses are inspected on silicon wafers by ellipsometry (VASE, JA Woollam). The coating minimizes leaching of cytotoxic materials from the magnet into the aqueous environment. Throughout all processes, the magnets are kept below their manufacturerrecommended maximum operating temperature of 80 °C. Probe station micropositioners (Cascade Microtech), coupled with glass micropipettes, are used for microscale fabrication. A straight pipette with 30 μm aperture (WVI) is used to apply epoxy to the flat-top pillar and a 45° bent pipette with 135 um aperture (Clunbury Scientific) is used to align and assemble magnets. Light vacuum (<1 psi) is applied on the straight pipette near UV-curable epoxy

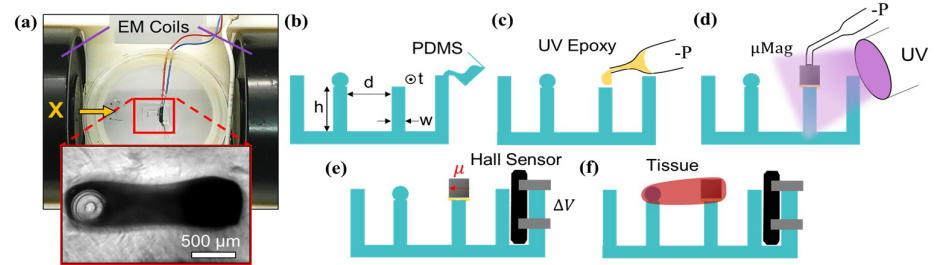


Figure 2: Fabrication: (a) device holder with self-assembled, (b) Polydimethylsiloxane (PDMS) microstructure, (c) application of UV epoxy, (d) magnetic functionalization, (e) assembly of Hall sensor, (f) assembled microtissue.

(NOA81, Norland Adhesives) to load the pipette. The pipette is brought into contact with the top of the flat pillar and vacuum is controllably decreased to deposit a few microliters on top of the pillar. Next, the micromagnet is held on a stationary vertical glass slide, oriented horizontally by an external magnet. The tip of the bent pipette is brought into contact with the top of the magnet, and vacuum (>2 psi) is pulled. The external magnet is removed so that the micromagnet can be positioned and oriented on the flat-top pillar (Fig. 2d), where the epoxy is spot cured by focused UV light (Bluewave, Dymax).

The magnetically functionalized PDMS structure is centered in a standard 35 mm petri dish (Falcon) and PDMS is poured around the structure and cured to fix position. For detection experiments, a Hall sensor (Allegro 1359) is easily inserted into a predesigned pocket in the PDMS mold (Fig. 2e). Leads carrying power and output signal are soldered and passivated using PDMS. The leads extend from the sensor and out of the petri dish through small holes that are resealed with epoxy.

At this point, the cell culture and tissue assembly procedure is conducted as described by Boudou, et. al for larger, 1 mm tissues [9]. The microtissue is cultured such that cells in a Fibrin gel self-assemble around the pillars, compacting to form a condensed microtissue. Fig. 2f illustrates this microtissue spanning the pillar tops of a functionalized device. Fig. 2a (inset) shows a microscope image after the PDMS microstructure is functionalized by both a magnet and microtissue. The tissue self-assembles at the tops of the pillars, around both the PDMS sphere (left) and magnet (right).

Device Holder

The petri dish is press-fit into a 3D printed holder, orienting and centering it between two concentric electromagnets (Uxcell P50/27). The holder is designed, so to allow simultaneous optical access by a brightfield microscope (Fig. 2a). To monitor multiple devices for long periods of time, the holders are placed in an incubator (37 °C, 5% CO₂). The wires are carried through a port to processing and recording equipment outside.

METHODS

Magnetic Field Design and Characterization

The coils are wired in an antiparallel configuration, giving rise to a gradient magnetic field and zero uniform field in the center of the petri dish, as illustrated by Fig. 3a, when the current is 300 mA. A single coil is characterized along its central axis (black squares). The magnetic field extending from the center of an electromagnetic coil is given by Eq. 1, where: \overline{B}_{coil1} is uniform magnetic field along the central X-axis, N is number of turns, k is the relative permeability of the core, M_0 is the magnetic permeability of air, R is the radius of the coil, I is the current, and \bar{X} is the distance from the center of the coil, along its central axis (see Fig. 3b). The experimental data in Fig. 3a is fit by Eq. 1 (black, dashed).

$$\vec{B}_{coil1} = N \frac{kM_0}{4\pi} \frac{(2\pi R^2)I}{(\vec{X}^2 + R^2)^{3/2}}$$
 (1)

Since the two coils are identical, but the second coil is reversed in direction and spaced by a separation, d, from the first coil, the second coil's magnetic field, \overline{B}_{coil2} , can be calculated from Eq. 1 by plugging in new X-coordinates in Eq. 2. The second coil is also opposite in sign from the first because the coils are in the anti-parallel configuration (same sign would be parallel).

$$\vec{B}_{coil2} = -f(\vec{B}_{coil1}) = -\vec{B}_{coil1}(-\vec{X} + d)$$
 (2)

 $\vec{B}_{coil2} = -f(\vec{B}_{coil1}) = -\vec{B}_{coil1}(-\vec{X} + d)$ (2) The uniform field profile, B, can be calculated by Eq. 3 as the gradient field profile, ∇B_x , can be calculated by its spatial derivative along the X-axis in Eq. 4. Both Eq. 3 and 4 are plotted in Fig. 3a, calculated from the single coil experimental data (red, blue respectfully).

$$B = B_{coil1} + B_{coil2} \tag{3}$$

$$\vec{B} = \vec{B}_{coil1} + \vec{B}_{coil2}$$

$$\nabla \vec{B} = \frac{d\vec{B}}{d\vec{X}}$$
(4)

The antiparallel system is specifically designed so that the magnet will feel a force on one axis without torque, and the Hall sensor will detect the micromagnet position, having minimal interference from a very low uniform field. A uniform magnetic field, \overline{B} , would apply an unwanted torque, T, to a magnet of moment \overline{M}_{mag} by Eq. 5 [11], and so is minimized by design. A gradient magnetic field imposes a force, \vec{F} , on the magnet of moment \vec{M}_{mag} by Eq. 6 [11]. It should be noted that the volumetric region where this occurs is small (<5 mm), and instabilities in the magnetic field exist in off-axis directions.

$$\vec{T} = \vec{M}_{mag} \times \vec{B} \tag{5}$$

$$\vec{F} = \vec{M}_{mag} \cdot \nabla \vec{B} \tag{6}$$

The micromagnet has a moment, \overline{M}_{mag} , of 15 μ J/T calculated from experimental data and confirmed by simulation. Experimental magnetic field, \overline{B}_{mag} , is gathered from a Hall sensor along the central axis of the micromagnet, \vec{r}_{mag} . Magnetic permeability of air, M_0 , is constant, so the moment of the micromagnet, \overline{M}_{mag} , is extracted by a fit using Eq. 7 for that of a magnetic dipole [11]. This is confirmed by a simulation (FEMM) and a 250

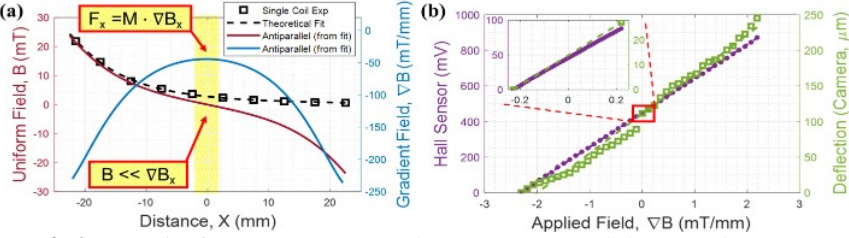


Figure 3: Design and characterization: (a) experimental measurement and theoretical fit of uniform and gradient magnetic fields, (d) characterization of gradient field actuation by camera and magnetic sensor.

µm cylindrical magnet of N52 grade. The yellow in Fig. 3a notes a region where the uniform field varies by less than 5%, minimizing interference on the Hall sensor. The sensor's close proximity to the micromagnet enables it to primarily detect the pillar position. Asymmetries in coil construction (number of turns, etc.), coil placement, sensor tip/tilt, sensor centering can vary in some setups. To further minimize interference in these cases, a dummy Hall sensor is placed nearby in the well and scaled in real time to subtract unwanted interference.

$$\overrightarrow{B}_{mag} = \frac{2M_0 M_{mag}}{4\pi} \left(\frac{1}{\overrightarrow{r}_{mag}}\right)^3 \tag{7}$$
 Eq. 7 may also be used to detect the position of the

Eq. 7 may also be used to detect the position of the magnet with the Hall sensor in Eq. 8. The micromagnet is spaced a distance away from the Hall sensor such that it can still be detected and small deflections can be approximated by a linear change in magnetic field (or Hall voltage). A constant, γ , expresses the sensitivity.

$$V_{Hall} = \gamma * r_{mag}$$
 (8)

Actuation and detection are characterized by statically actuating the magnet through a large range of deflection (> 200 μm) while recording camera images and Hall sensor outputs simultaneously (Fig. 4d). The gradient magnetic field is swept linearly from -2.4 to 2.4 mT/mm. The relationship between gradient field and deflection is found to be a linear least square fit, indicating good alignment of magnet assembly, minimal torquing, and a linear pillar spring constant. The relationship between gradient field and Hall voltage is also found to be linear, validating a small deflection approximation of the magnet. The sensitivity, γ , can then be calculated by a ratio of these two slopes, resulting in 3.4 mV/µm. A fine sweep is conducted in the central region (Fig. 3d inset), confirming a linear relationship with a smallest step size of 11 µT/mm resulting in 2.25 mV and 660 nm deflection.

Deflection Tracking with Microscope

An inverted brightfield microscope (Nikon Eclipse Ti), is used to track deflection of pillars when a microtissue is present. Settings are 5X magnification and 30 frames per second. A custom MATLAB script is used to track the deflection of the pillars in sequential image frames by tracking features with steep image gradients. When tissue is grown on the device (Fig. 2a, 4a and 4b), the magnet edges are obscured and deflection of a feature on the spherical pillar top is tracked. During actuation experiments, the deflection of the nonmagnetic pillar and the applied force on the magnetic pillar are used to calculate tissue strain (assuming linear elastic properties of the microtissue). This technique is useful for quick measurements (under a minute), but large microscope image files become burdensome for long-term monitoring.

Biological samples must also be transported into a separate microscope incubation chamber, risking contamination and requiring stabilization of sample temperature and humidity. **Signal Processing and Control**

A series of electronics are used to control the electromagnetic coils and record the Hall sensor signal. These can be configured for actuation only, detection only, open loop, and closed loop (as illustrated in Fig. 1). As described earlier, the entire system is capable of long-term measurement inside an incubator. The control circuit sits outside the incubator and consists of an SRS mainframe (SIM900) with a sequence of modules (SRS SIM module series).

For actuation, the electromagnetic coils are driven by an Arduino DUE (Adafruit). On-board digital-to-analog converters are used in combination with a coil-driving circuit (OPA548 EVM) for electromagnetic actuation. An arbitrary waveform (i.e. sinusoidal) is digitally specified inside the Arduino using a looping matrix reference scheme. Recall, the magnet may be actuated bidirectionally, providing tension and compression.

For detection, the raw Hall signal is offset (SIM983) to zero (Hall sensor nominal voltage is 2.5 V) and amplified (SIM911). A low pass, Bessel analog filter (SIM965) with 25 Hz cut off and 48 dB/oct roll-off is selected to attenuate high frequency noise. The dummy sensor can also be used for long – term measurements to eliminate drift due to temperature and humidity inside the incubator. The signal is scaled (SIM983) to a 0-3.3 V range to maximize the 12-bit resolution of the Arduino analog-to-digital converter. At this point, the measurement can be stored in a buffer and flushed to a data logger shield (Adafruit), for inspection later.

The open loop configuration is simultaneous actuation and detection. This is enabled by our design that minimizes magnetic interference. A dummy sensor within the same petri dish can be used to subtracted before amplifying in real-time from the Hall signal to reduce interference from temperature, humidity, nearby equipment, residual uniform field. To close the loop, an arbitrary waveform and detected waveform are iteratively combined in an algorithm based on the feedback desired. The control loop circuitry is capable of 620 µs temporal resolution when a separate Arduino is used for data storage.

RESULTS AND DISCUSSION

Cyclic magnetic actuation of a cardiac microtissue is demonstrated in Fig. 4a and b over 15 seconds, recorded by the microscope. Fig. 4a shows spontaneous beating of the

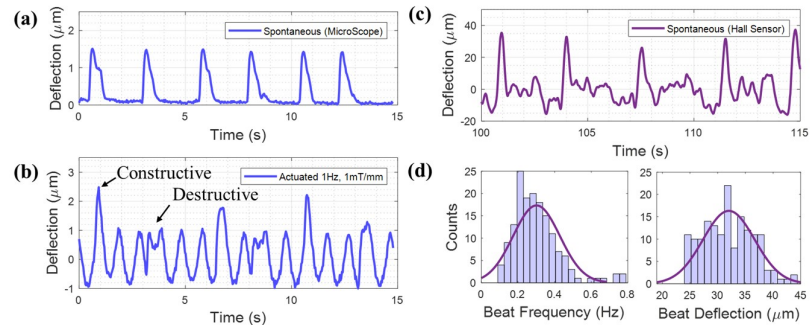


Figure 4: Actuation and detection of human induced pluripotent, stem-cell derived (hiPSC) cardiac tissue: (a) spontaneous beating recorded by microscope, (b) magnetic actuation and beating recorded by microscope, (c) long-term monitoring of spontaneous beating using non-contact sensor, (d) frequency and deflection histograms from hour long recording.

cardiac microtissue without actuation (after only 4-5 days of culture, 1-2 µm deflection is normal). The tissue deflects both pillars symmetrically with a typical profile comprising a steep increase followed by a slower relaxation. It is also typical for arrhythmic beat frequency at this stage, as can be identified by the smaller time period between the 5th and 6th peak. Such arrhythmias and small deflections can be artifacts of immaturity that may be improved by mechanical or other pacing [2,3]. The same tissue is used minutes later to gather the data in Fig. 4b. The magnetic pillar is actuated by a 1 Hz, 1 mT/mm peak-to-peak sinusoidal gradient magnetic field, resulting in a bidirectional, cyclic strain of 0.3%. Throughout actuation, the tissue beating can still be observed and analyzed by constructive and destructive deflections labeled on the plot. While these are results from a single sample, further work is needed to increase alignment and/or decrease magnetic instabilities in order for this technology to be realized in a high-throughput, tissue testing application. Misalignment of some samples can cause torsion to dominate deflection, resulting in a non-ideal actuation.

Detection for one hour inside an incubator is shown in Fig. 4c and analyzed in Fig. 4d. This sample (different than Fig. 4a and b) is measured on day 10 of maturation and so larger beat deflections are normal. A dummy sensor is not used to subtract artifacts from temperature, humidity, or nearby equipment, giving rise to the low signal to noise in Fig. 4c. Information from over 1000 spontaneous contraction peaks may be used, however, to gather long-term monitoring information about trends in beat frequency and beat deflection. A histogram of beat frequency is shown, fit by a normal distribution with a mean of 0.30 Hz and standard deviation of 0.13 Hz. Similarly, a histogram of beat deflection is shown with a mean of 32.0 µm and standard deviation of 4.6 µm.

CONCLUSIONS

The results shown herein demonstrate a biocompatible platform that substantially opens the design space of a micromechanical environment of biological tissues. A system was designed with arbitrary waveform, bidirectional actuation, simultaneous detection with minimized interference, and an opportunity for controlled tissue strain experiments. Both open loop and closed loop experiments offer exciting, new experimental design. In an open loop case, effects of substrate stiffness [8], static

stress [2,6], mechanical pacing [3,5,6], and tissue strain characterization (such as the tissue length-dependent Frank-Starling relationship) [2] can be dynamically studied. In a closed loop case, all these open-loop environments and many mechanical parameters (spring constant, damping, viscoelasticity, etc.) can be altered in response to real-time tissue behavior. The interdisciplinary combination of such applied physics techniques and biology offer critical solutions to cardiac tissue engineering, with the promise of a completely active environment to study maturation in cardiac microtissues.

ACKNOWLEDGEMENTS

The authors would like to thank Jourdan Ewoldt and Paige Cloonan for cell culture preparation and Professor Anna Swan for the use of her customized probe station. This work was supported by the NSF CELL-MET ERC award no. 1647837.

REFERENCES

- [1]. Chen, Christopher S., et al. *Annu. Rev. Biomed. Eng* 6, pp. 275-302, 2004.
- [2]. J.-L. Ruan, et al. Circulation 134, pp. 1557-1567, 2016.
- [3]. RB, Kacey, et al. Nature, 556.7700, pp. 239, 2018.
- [4]. Zhao, Yimu, et al. Cell, 176.4 pp. 913-927, 2019.
- [5]. Imboden, Matthias, et al. *Nature Comm*, 10.1, pp. 834, 2019.
- [6]. F. Xu, et al. Lab on a Chip, 105, pp. 1293-303, 2013.
- [7]. KS. Bielawski, et al. *Tissue Engineering*, 22.10, pp. 932-40, 2016.
- [8]. E. Corbin, et al. ACS applied materials & interfaces, 2019.
- [9]. T. Boudou, et al. *Tissue Engineering Part A*, 18.9-10, pp. 910-919, 2011.
- [10]. Stange, Alexander, et al. *Microsystems & nanoengineering*, 5.1, pp. 14, 2019.
- [11]. De Lacheisserie, et al. Springer Science & Business Media, 1, 2005.

CONTACT

*J. Javor, jjavor@bu.edu